

COMPUTER-AIDED OPTICAL PLASMA POSTPROCESSING APPLIED ON MODEL SPARK GAPS

E. PETERS*, B. WEBER, T. H. KOPP, M. KURRAT

Technische Universität Braunschweig elenia Institute for high voltage technology and power systems, Schleinitzstrasse 23, 38106, Braunschweig, Germany

* e.peters@tu-braunschweig.de

Abstract. Spark gaps are used as surge protective devices (SPD class 1) for low voltage grids protection against surge currents and overvoltages. For practical research of the narrow gap plasma of spark gaps, high-speed camera recordings are used in modified transparent test models. In this test setup, current densities of 10^{10} A/m² are generated. In order to optimize and automate the evaluation process of camera recordings, an image analysis tool is developed further in this contribution. After basic image improvement and segmentation, this research optimizes a detection algorithm for plasma location and distribution. As a result, the known plasma distribution gives access to significantly more information about the plasma behaviour and the spatial distribution of radiation.

Keywords: high speed camera, surge current, optical analysis methods, plasma detection.

1. Introduction

For higher reliability in electrical distribution grids with regard to surge current events, surge protective devices (SPDs) are used. Surge current arresters (class 1) are used especially for the protection of high-energetic transients. The state of the art for SPDs designed for low voltage grids, is to quench the electrical arc, into a narrow gap. This leads to an intended current limiting, due to a lower cross section and a forced ablation of the chamber walls. This generates plasma cooling, which increases the arc voltage.

There is an extensive research history, so many researchers have been intensively investigating theoretical plasma properties [1–4]. To support the plasma community, this paper provides experimental data for transient plasmas. For a better understanding of the high current phase during a surge current (8/20 μ s, IEC 62475) and the subsequent recovery phase, advanced methods for analysis are used. For this purpose, optical methods are used. The main advantage of these methods are: an undisturbed measurement of the plasma which also increases the reproducibility of data analysis. It is highly beneficial that these methods are non-invasive and feedback-free. In addition, a visualisation of the plasma distribution is obtained, which improves data interpretation.

The paper consists of the experimental setup for the spark gap, the image analysis tool (IAT) and the application of the IAT.

2. Experimental Setup

A measurement setup of a model spark gap for plasma observation with a high-speed camera (HSC) is developed. The electrical circuit with HSC and data acquisition is given in Figure 1.

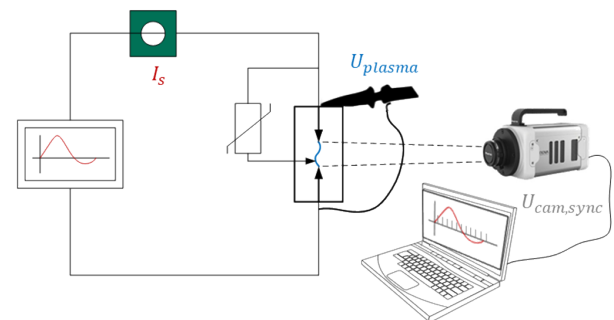


Figure 1. Surge current circuit and data acquisition

The current source on the left is a surge current generator, generating a bipolar surge current up to 10 kA according to IEC 62475. The front time of the transient waveform is 8 μ s and the time to half-value is 20 μ s. This waveshape is used to test surge current arresters according to international standard (IEC 61643-11).

The current I_s is measured due to high transient behaviour via the magnetic field monitor (type 1423, Pearson). The voltage at the connectors of the spark gap U_{plasma} is measured with a high voltage probe (type PHV 1000, manufacturer PMK) with a divider ratio of 100:1. Also the synchronisation signal of the HSC is recorded. In this setup the plasma is recorded with the HSC (type Photron FASTCAM NOVA S6) with the parameters:

- bit-depth of 12 bit
- framerate of 320 kfps
- resolution of 128 x 64 pixel
- integration time of 0.2 μ s

During surge currents in the timescale of some 10 μ s high electrical power is applied. This leads to a high

plasma pressure of several 10 MPa with intensive radiation due to high plasma temperatures [5, 6]. Therefore, it is necessary to reduce the radiation intensity with aperture and neutral density filters. In this setup neutral density filter of ND 3.0, ND 0.6, ND 0.6 are combined.

For the recording of electrical data an acquisition system (type AD3000, Highvolt) is used and connected via fibre optic cable to ensure decoupling. It provides a sampling rate of 100 MS/s with a 14-bit amplitude resolution.

The plasma ignition is established using a surface discharge device (SDD) which is connected in series with a varistor (type LS40K440QP, EPCOS-TDK). This enables a current-dependent ignition of the spark gap and is called ignition circuit. The ignition circuit is connected to the anode and to the SDD. The SDD represents a third electrode of the spark gap, which is located in front of the cathode. Therefore the ignition circuit bypasses the plasma chamber and is routed directly in front of the cathode to achieve a current-dependent commutation of the surge current into the plasma chamber (see Fig. 1). After initiating a plasma at the SDD, the plasma chamber is ionized. This leads to a decrease in the resistance of the chamber, which supports the commutation process. The detailed functional principle can be taken from [7]. Figure 2 shows the device under test, the model spark gap.

The spark gap consists of two tungsten copper electrodes (80%/20%) and one surrounding chamber wall. The bottom part is made out of the plastic polyoxymethylene (POM) and the top part of the chamber wall (the front) is made out polymethylmethacrylate (PMMA), in order to obtain optical access. The transparent part of the model spark gap is not shown in Fig. 2. The dimensions of the plasma chamber are 10 mm by 10 mm area and a height of 1 mm. In the center between the electrodes are two outlet ducts to enable a plasma flow into the surrounding environment. The isolation of the current feed is required to insulate the housing around the model spark gap. The second part of the Fig. 2 shows a vertical cross section perpendicular to the current flow, which is important for the section 3.1.2.

3. Optical plasma detection

High speed imaging with the consideration of plasma characteristics can be used as a method for non-invasive and feedback-free plasma diagnostics. Different properties, such as the spectral distribution of radiation and the pressure range, must be known in order to allow conclusions from the image alone. These properties were investigated in previous works [5–8].

The plasma temperature is depended on the surge current amplitude [6]. Due to the transient excitation many charge carriers must be available in a timescale of sub microseconds. Recent investigations show that

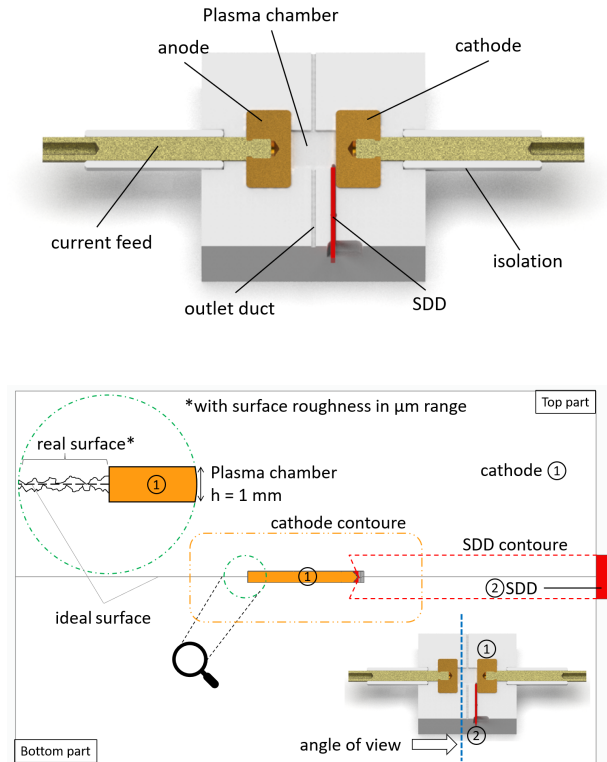


Figure 2. Top: Horizontal cross section of Model spark gap with surface discharge device (SDD), Bottom: schematic of model spark gap with vertical cross section at red solid line (along the current direction)

a surge current results in high pressure of several MPa [5] and a high temperature in the range of 20–30 kK [6]. Due to the above-mentioned processes, the radiation flux increases, which is digitized by the camera and thus leads to an increase in the brightness of the images. The HSC can therefore be used to determine a relative measurement of the plasma state. It was found that the plasma has a low optical depth and the radiance can be assumed as a grey body radiator [8, 9]. The presented method in this contribution will show a high level of reproducibility of the results due to application of automation in image recognition.

3.1. Functional principle of the image analysis tool

The image analysis tool (IAT) is written in the open-source software python making a scientific exchange more viable. In order to ensure an analysis of the pixels on the images, it must be ensured that the sensor does not work in saturation (4095, 12-bit). Otherwise, information for the processing of the data is cut off.

The image data is converted into binary data by a 12-bit adapted Otsu-method, which simplifies data processing for subsequent steps and highlights the relevant image regions. The Otsu-method is known for 8-bit recordings and can be described as global dynamic threshold procedure [10]. A global dynamic

threshold proved to be suited for plasma recordings with a high radiation intensity and dark background, because of its robustness and adaptability [11].

3.1.1. Plasma detection and localisation

This subchapter focuses on detecting and locating plasma within the chamber, which is shown in the following graphic.

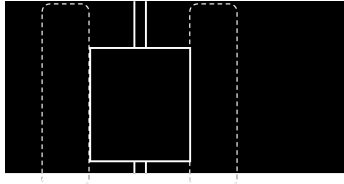


Figure 3. Ideal image with contacts in dashed lines and plasma chamber and outlet ducts in solid lines

At first, after converting the raw data into binary data, it is optimized by binary morphological operations. Every image is a 2-D array with a digital value of the radiation in a cell called pixel. A binary structure is formed, a 3×3 array, so that only the direct neighbors of the center are considered for the calculation. This binary structure is used for the following opening and closing algorithms. Opening, therefore, removes objects smaller than the structuring element and closing fills holes smaller than the structuring element. In combination a noise reduction is achieved for every frame from the recording [10].

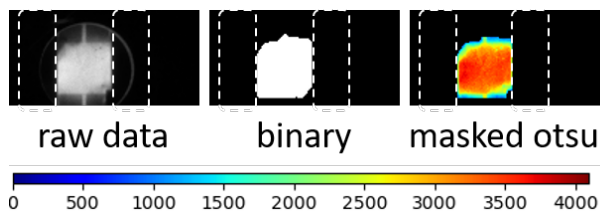


Figure 4. Steps of object recognition, images contain contacts in dashed lines. Image resolution 64×128 pixels

In Fig. 4 the first steps of data processing are presented. On the left side, there is a raw image from the HSC. Further on, the 12-bit Otsu-method is used to identify the plasma [11, 12]. As a result, the binary image is used as a mask for the original image to convert only the relevant pixels into the masked Otsu image. A color code is applied, which converts high pixel values to red and small pixel values to blue according to the illustrated scale. The systematic processing of the optical data is the basis of a correct image recognition, which is necessary for a later analysis of the plasma. It should be noted that the image processing algorithms do not change the brightness values in the cells. Each image series, consisting of n images, is read in, stored in a data structure and prepared in the described way for increasing reproducibility. During the high current phase of the surge

current with typical 320 kfps at the desired resolution 11–13 images are recorded.

3.1.2. Determination of the plasma area

The next step is an improved determination of the plasma area inside the plasma chamber based on the boundary box from section A. It is described that the plasma area is determined by the intensity via the Otsu-method. Parameters of Otsu-method change for every image, which is the aim of a dynamic threshold method. Due to the high pressure of the plasma in the range of several MPa, it can be pressed into the cavity between the top and bottom parts of the model spark gap (see Fig. 2). Fig. 5 shows this effect.

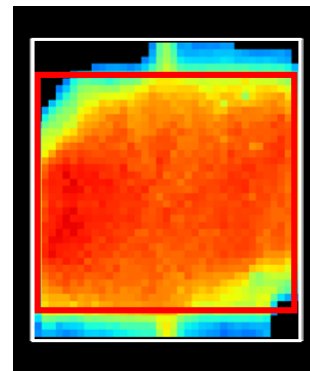


Figure 5. Boundary box of detected plasma (white) (horizontal 38 px, vertical 42 px) via Otsu and trimmed boundary box (red)

Fig. 5 shows the intensity distribution of the plasma of a 10 kA surge impulse. In addition, the white boundary box of detected plasma via the Otsu-method is shown. The red box shows the improved recognition, the so called trimmed boundary box. The adjustment via the red box results in a minimization of the error of the detected plasma surface, which recognizes the plasma chamber of the real setup and thus improves the automated evaluation.

There are a few pixels outside the red box, which do not belong to the current driven plasma in the chamber. The cause of this effect is to be found in the preparation of the model, as it consists of two parts that are pressed together. The tolerances of the surfaces of the model spark gap generate very thin cavities. The contact pressure of the parts cannot be increased arbitrarily, otherwise it leads to internal stresses which damage the model spark gap (see Fig. 2). This leads to plasma in the described cavity, which has to be removed by image processing for the calculation of the current carrying area. As a result the current flow I_s in this very thin cavity in the area outside the trimmed boundary box has a negligible crosssection (plasma chamber height is 1 mm, height cavity in the range of $\approx \mu\text{m}$). This theory is supported by the temperature profile of a plasma, which decreases radially from the hot core [13, 14]. A decreasing temperature results in a lower current density (J_s) in this region. Also, a second effect is that

the hot gas is led out through the outlet duct, which is correctly recognized as plasma by the algorithm. The plasma in the outlet duct leaves the plasma chamber between the electrodes and is therefore no longer part of the current flow between the electrodes (geometrical reasons) and can thus also be neglected.

All in all, this creates an undefined area for the further analysis. The area outside the red box can be assumed to be a non-conductive area of the plasma based on the 2-zone model. This assumption is valid due to high current densities which causes a high conductive, hot plasma core and a vapor zone with neglectable conductivity. This concept based on the fact that the input energy is converted into radiation losses (in form of grey-body radiation) which result in wall ablation. [15–17]

So this tool results in a improved method that allows a better description of the current flow in the defined area between the electrodes. This excludes the tolerances through the experimental setup and the part of the plasma that is blown out.

For the calculation of the trimmed boundary box, a semi-automated algorithm is used. The aim is to determine the boundaries of the plasma chamber, which is achieved through an optimisation process of two loss functions B_1 and B_2 , where B_1 describes the area of the box and B_2 the inverse pixel sum of the area.

$$\min(B) = \min(w_1 \cdot B_1 + w_2 \cdot B_2) \quad (1)$$

Both functions can be weighted by a user input by w_1 and w_2 and are applied on the top boundary and bottom boundary. w_1 and w_2 can be set in a single training step. These weights are applied to the entire measurement set with the same conditions (current amplitude, camera settings). Both limits are calculated in the same way, therefore only the calculation of the top boundary is described in the following. The first loss function B_1 represents the ratio of the trimmed area (red box) to the area of the entire boundary box (white box). For every iteration of the algorithm on the resulting box is reduced by one row. So the area of the trimmed area is reduced by one row while the total area remains constant, which indicates a monotonically decreasing function for B_1 . In the first iteration step both areas are the same, so the start value can be set via the weight w_1 . The aim is an area reduction; the higher the ratio, the higher the loss. Hence, we try to minimize this ratio:

$$B_1 = \frac{\text{trimmed area}}{\text{total area(box)}} \quad (2)$$

The loss function B_2 has its aim to preserve pixel with high values, which correlate with a significant amount of information. This loss slows down object trimming. It represents the object retention. In the first iteration step both sums are the same, so the starting value of the function B_2 is always zero. With increasing iteration index, more and more pixel cells are removed. The higher the cell values the higher

the values of the loss function B_2 . So the function B_2 results in a monotonously increasing function. The slope can be adjusted via the weight w_2 .

$$B_2 = 1 - \frac{\text{trimmed area pixel sum}}{\text{total area pixel sum(box)}} \quad (3)$$

The minimum of the function B (see. eq. (1)) is the calculated reduction of the boundary box. Therefore the local minimum of this function represents an optimum between a minimum area with maximum pixel values. For the used example data of a 10kA surge current and HSC settings from section 2, weights in height $w_1 = 0.6$ and $w_2 = 1$ were set.

3.2. Application of the method

With the methodology presented in chapter 3.1, the radiation of the plasma can be processed in a target-oriented approach with the aim of describing the effective current-carrying area. Therefore, the presented trimmed boundary box is used.

The example data shown in Fig. 6 is taken from a 10kA surge impulse. The before after comparison between the masked Otsu image (full image) and the trimmed boundary box can be seen via the histograms. The rectangle in red marks the trimmed image. At the top there is the histogram of the inner part of the image (trimmed box).

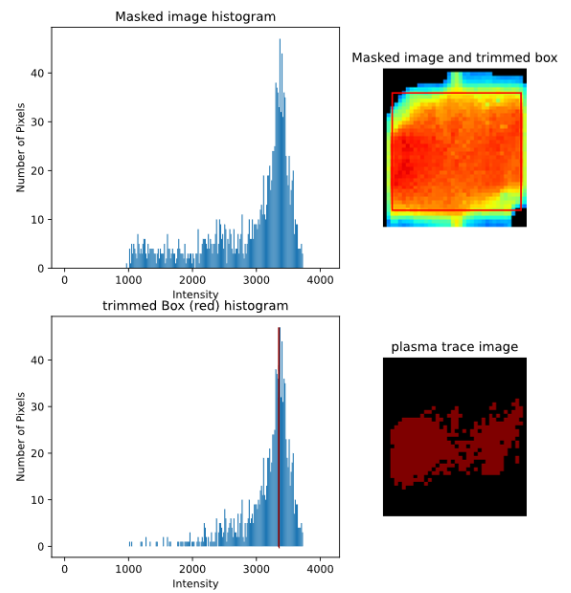


Figure 6. Example electrical Data, $I_s = 10\text{ kA}$, top: masked histogram with image and trimmed box, bottom: histogram of trimmed box and brightest 90% of the radiating area

It can be seen that the high intensity range is reproduced identically. The range below 2500 is clearly reduced in the trimmed histogram, which suggests that the radiation from the edge region is suppressed.

As a result, it can be noted that focusing on the current-carrying region results in advantages for the

period after the current zero crossing. Here, the radiation is much weaker and the influence from the noise of the edge areas has a significantly higher effect (see Fig. 7).

Furthermore, the intensity distribution cross to the flow direction is particularly high in the center and lower at the edges due to the cooling effect of the chamber wall. This is in accordance with the literature [13, 14].

Another benefit is that hotspots can be better classified. These more intense areas of the plasma are a representation of the hot core. This is shown in the plasma trace image, where the brightest 90% of the pixel values are displayed. The combination of the distribution of the number of pixel and plasma trace image improves the visualization of radiation intensive zones. In fig. 6 at the bottom, only pixel values to the right of the red threshold line in the histogram below are shown in the picture plasma trace image. So with this results, it is possible to enable a representation of how the local pattern of the most radiation-intensive pixels are distributed. From this, it is expected in the future to generate results, that can better assess the cooling effect of different geometric changes or chamber wall materials based on this distribution.

Fig. 7 shows an image of the maximum undershoot current of 1.8 kA:

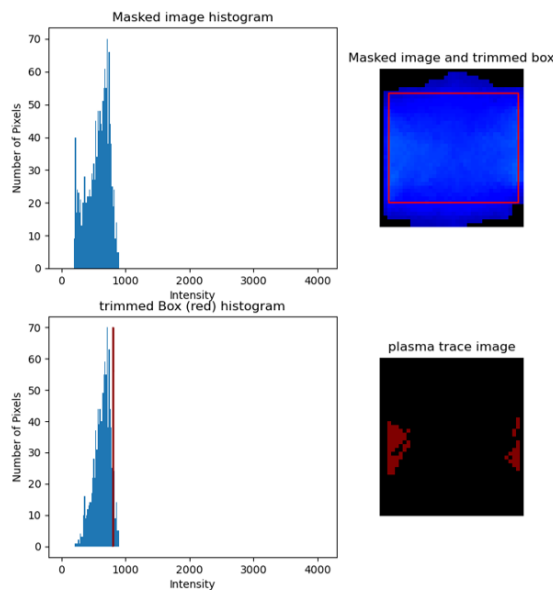


Figure 7. Example electrical Data, $I_s = -1.8 \text{ kA}$, top: masked histogram with image and trimmed box, bottom: histogram of trimmed box and brightest 90% of the radiating area

It can be noted, that the distribution of the plasma in the chamber is approximately homogeneous even for lower currents (comparison to 10 kA in fig. 6). This is true for the entire series of images up to just before the current zero crossing. But the brightest 10% does change alot. So the calculated place trace image is

helpful to show the hot zones. In the following figure 8 all histograms are shown over the whole period of the pulse:

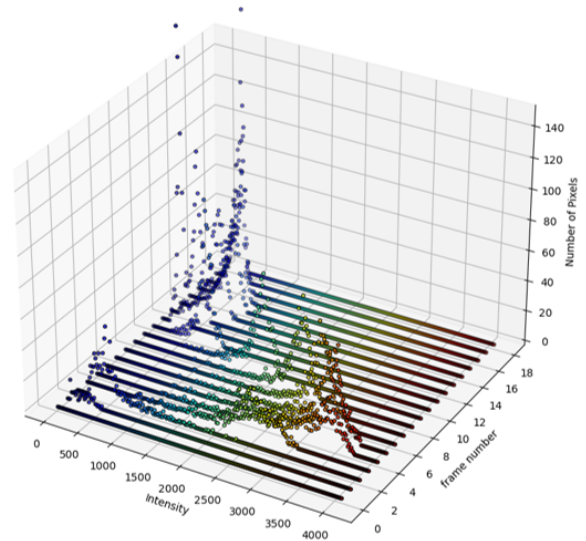


Figure 8. Example histogram over time of the trimmed box with intensity, frame number and number of pixels per recording

This figure shows intensity over the number of pixels as an histogram. Along the y-axis there is a time parameter as frame number (the plasma is sampled every $3.125 \mu\text{s}$). This illustration allows the user to see the overall distribution of low and high regimes of the all recordings. So more intense radiation occur at the images 4 to 8. The current zero crossing is at image 11. After that, a less intense brightness can be seen due to the undershoot. The effect of the improved recognition by the trimmed box is particularly noticeable in the area of the high-current phase (recording 4–8), since here the number of pixels with an intensity of less than 1500 is almost zero.

4. Conclusion and outlook

In summary, by improving the detection of the current-carrying region via the trimmed box, a method is available that can be used for non-invasive and feedback-free plasma diagnostic. A major advantage is that a single training step is required to adaptively filter out the relevant area in otherwise identical settings. The main benefit of this tool is a further reduction of an error in the recognition of the current carrying surface of the plasma with a high reproducibility due to the semi automated analysis. Furthermore, the existing pixel values in the cells are not changed. The method can also be applied in the range of circuit breaker plasma, if they are confined in a narrow gap.

The distant aim in the future is to develop a local description of the plasma physical quantities. For this, the first step is to establish a relationship between the radiating surface of the plasma and the current distribution. Therefore, the current carrying region is determined by the presented tool.

References

- [1] Y. Cressault, R. Hannachi, P. Teulet, et al. Influence of metallic vapours on the properties of air thermal plasmas. *Plasma Sources Science and Technology*, 17, 2008. doi:10.1088/0963-0252/17/3/035016.
- [2] A. D'Angola, G. Colonna, C. Gorse, and M. Capitelli. Thermodynamic and transport properties in equilibrium air plasmas in a wide pressure and temperature range. *The European Physical Journal D*, 46(1):129–150, 2008. doi:10.1140/epjd/e2007-00305-4.
- [3] A. B. Murphy. Transport coefficients of air, argon-air, nitrogen-air and oxygen-air plasmas. *Plasma Chemistry and Plasma Processing*, 15(2):279–307, 1995. doi:10.1007/BF01459700.
- [4] L. Zhong, X. Wang, Y. Cressault, et al. Influence of metallic vapours on thermodynamic and transport properties of two-temperature air plasma. *Physics of Plasmas*, 23(9):093514, 2016. doi:10.1063/1.4963245.
- [5] T. Runge, T. H. Kopp, M. Kurrat, et al. Experimental investigations on plasma pressure in a narrow gap for short time currents. In *International Conference on Electric Contacts Edinburgh, Great Britain*, 2016.
- [6] T. Runge, St. Franke, S. Gortschakow, and M. Kurrat. Optical investigations on plasma temperature estimation in a model spark gap for surge currents. *Plasma Physics and Technology*, 4(2):108–111, 2017. doi:10.14311/ppt.2017.2.108.
- [7] T. Runge, T. Krause, T. H. Kopp, et al. Measurement of plasma pressure in a narrow gap for different surge currents. In *International Conference on Gas Discharges and their Applications, Nagoya, Japan*, 2016.
- [8] T. Runge. *Plasmaeigenschaften in Funkenstrecken unter Stoßstrombelastung*. Dissertation, Technische Universität Braunschweig, 2018.
- [9] T. H. Kopp, E. Peters, and M. Kurrat. Estimation of current density using high-speed-camera recordings in a model spark gap during surge currents. *Plasma Physics and Technology*, 6(1):60–64, 2019. doi:10.14311/ppt.2019.1.60.
- [10] R. C. Gonzalez and R. E. Woods. *Digital image processing*. Pearson/Prentice Hall, Upper Saddle River, NJ, 3. ed. edition, 2007 [erschienen] 2008. ISBN 978-0131687288.
- [11] N. Otsu. A threshold selection method from gray-level histograms. *IEEE Transactions on Systems, Man, and Cybernetics*, 9(1):62–66, 1979. doi:10.1109/TSMC.1979.4310076.
- [12] B. Weber, D. Gentsch, T. Pieniak, and M. Kurrat. Software-based processing of the radiation intensity distribution of high-current vacuum arcs between transversal magnetic field contacts. In *28th International Symposium on Discharges and Electrical Insulation in Vacuum (ISDEIV)*, pages 495–498. IEEE, 2018. ISBN 978-1-5386-4375-4. doi:10.1109/DEIV.2018.8537111.
- [13] M. Becerra, J. Pettersson, S. Franke, and S. Gortschakow. Temperature and pressure profiles of an ablation-controlled arc plasma in air. *Journal of Physics D: Applied Physics*, 52(43):434003, 2019. doi:10.1088/1361-6463/ab34b6.
- [14] R. Methling, St. Franke, D. Uhrlandt, et al. Spectroscopic study of arc temperature profiles of a switching-off process in a model chamber. *Plasma Physics and Technology*, 2(2):163–166, 2015.
- [15] E. Z. Ibrahim. The ablation dominated polymethylmethacrylate arc. *Journal of Physics D: Applied Physics*, 13(11):2045–2066, 1980. doi:10.1088/0022-3727/13/11/015.
- [16] A. D. Stokes and L. J. Cao. Ablation arcs. i. arcs in ice. *Journal of Physics D: Applied Physics*, 22(11):1697–1701, 1989. doi:10.1088/0022-3727/22/11/019.
- [17] L. Müller. Modelling of an ablation controlled arc. *Journal of Physics D: Applied Physics*, 26(8):1253–1259, 1993. doi:10.1088/0022-3727/26/8/015.